Resonant inelastic X-ray scattering using a miniature dispersive Rowland refocusing spectrometer

Alexander S. Ditter,[a,b] William M. Holden,[a] Samantha K. Cary,[b] Veronika Mocko,[b] Matthew J. Latimer,[c] Erik J. Nelson,[c] Stosh A. Kozimor[b]* and Gerald T. Seidler[a]*

[a]Department of Physics, University of Washington, PO Box 351650, Seattle, WA 98195-1560, USA, [b]C-IIAC, Los Alamos National Laboratory, PO Box 1663, Los Alamos, NM 87545, USA, and [c]Stanford Synchrotron Radiation Lightsource, SLAC National Accelerator Laboratory, 2575 Sand Hill Road, Menlo Park, CA 94025, USA. *Correspondence e-mail: stosh@lanl.gov, seidler@uw.edu

Received 6 June 2019
Accepted 25 January 2020

Edited by S. M. Heald, Argonne National Laboratory, USA

Keywords: RIXS; XES; X-ray spectroscopy; instrumentation.

X-ray absorption spectroscopy (XAS) beamlines worldwide are steadily increasing their emphasis on full photon-in/photon-out spectroscopies, such as resonant inelastic X-ray scattering (RIXS), resonant X-ray emission spectroscopy (RXES) and high energy resolution fluorescence detection XAS (HERFD-XAS). In such cases, each beamline must match the choice of emission spectrometer to the scientific mission of its users. Previous work has recently reported a miniature tender X-ray spectrometer using a dispersive Rowland refocusing (DRR) geometry that functions with high energy resolution even with a large X-ray spot size on the sample [Holden *et al.* (2017). *Rev. Sci. Instrum.* **88**, 073904]. This instrument has been used in the laboratory in multiple studies of non-resonant X-ray emission spectroscopy using a conventional X-ray tube, though only for preliminary measurements at a low-intensity microfocus synchrotron beamline. This paper reports an extensive study of the performance of a miniature DRR spectrometer at an unfocused wiggler beamline, where the incident monochromatic flux allows for resonant studies which are impossible in the laboratory. The results support the broader use of the present design and also suggest that the DRR method with an unfocused beam could have important applications for materials with low radiation damage thresholds and that would not survive analysis on focused beamlines.

1. Introduction

The more complete utilization of fully photon-in/photon-out X-ray spectroscopies in the tender X-ray regime (2–5 keV) shows great scientific promise (Robba *et al.*, 2017; Kavčič *et al.*, 2016; Kvashnina *et al.*, 2014; Butorin, 2000; Groot & Kotani, 2008; Glatzel & Bergmann, 2005; Schülke, 2007; Vitova *et al.*, 2013). Despite the high impact demonstrated for these spectroscopic studies, the task of expanding material type compatibility and experimental access throughout the scientific community faces numerous challenges. There exists both logistical barriers in the relatively small number of high-flux beamlines operating in the tender X-ray range [*e.g.* ESRF 12-ID, 26-ID; SSRL 4-3, 6-2; NSLS II 7-ID; KARA (previously ANKA) INE-BL, CATACT] and also technical barriers in the design and operation of the required X-ray emission spectrometers (Kavčič *et al.*, 2012; Welter *et al.*, 2005; Hudson *et al.*, 2007; Dolgih *et al.*, 1984; Zimina *et al.*, 2017). Key technical considerations include compatibility with beamline design and vacuum systems, mitigation of beam damage, minimizing air paths to reduce absorption, and the complexity and cost of spectrometer development.

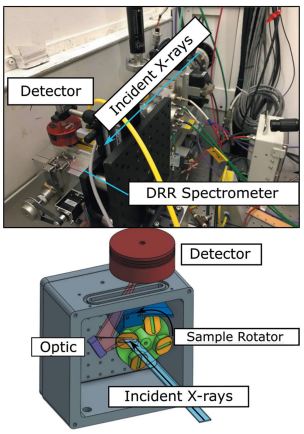

© 2020 International Union of Crystallography

For these reasons, recent work in laboratory-based X-ray emission spectroscopy has provided an interesting advancement (Holden *et al.*, 2017). Those authors developed an extremely compact tender X-ray emission spectrometer using the dispersive Rowland refocusing (DRR) geometry that largely removes source size effects on spectrometer energy resolution. While the removal of source-size effects has enabled the steady application of such instrument in the laboratory environment with only a conventional, unfocused X-ray tube source (Cossairt *et al.*, 2018; Stein *et al.*, 2018; Holden, Seidler & Cheah, 2018), the small size and compatibility of the equipment with either helium or vacuum environments suggests the versatility for synchrotron application. However, the study by Holden *et al.* gave only a preliminary investigation at a low-flux beamline. Here, we provide a broader assessment of the miniature DRR spectrometer in synchrotron applications, where we use an unfocused wiggler at the Stanford Synchrotron Radiation Laboratory (SSRL) on beamline (BL) 4-3 to perform resonant inelastic X-ray scattering (RIXS) studies in the tender X-ray regime [sulfur (S) $K\alpha$, S $K\beta$ and uranium (U) $M\beta$ RIXS]. The instrument performance was successful and showed good potential use at other high-flux tender X-ray beamlines, especially for studies of materials with low radiation damage thresholds.

2. Experimental

2.1. DRR spectrometer and installation at SSRL BL 4-3

The tender X-ray emission spectrometer operates in DRR geometry. As shown in Fig. 1(*a*), a point source on the Rowland circle ray-traces symmetrically to a point on the detection arc of the Rowland circle. In Fig. 1(*b*), a large source that is positioned significantly interior to the Rowland circle is seen by the analyzer as equivalent to a superposition of discrete source points of varying energy, resulting in spectral refocusing onto each point on a corresponding detector arc but without any imaging of the sample location, *i.e.* the detected spectrum is at least a significant spatial average, loosening sample preparation homogeneity constraints. Operation of a Rowland circle spectrometer with an extended source on the Rowland circle has been discussed by Huotari *et al.* (2011) and is common in plasma physics research (Glenzer *et al.*, 2003; Glenzer & Redmer, 2009; Woolsey *et al.*, 2011; Valdivia *et al.*, 2018, 2015; Suggit *et al.*, 2010; Plateau *et al.*, 2012; Matlis *et al.*, 2006; Mao *et al.*, 2012; Labate *et al.*, 2012; Kritcher *et al.*, 2011; Hudson *et al.*, 2002; Hoidn & Seidler, 2014; Gamboa *et al.*, 2012) where combined imaging and spectroscopy is achieved.

Complete instrument details are given in our previous work (Holden *et al.*, 2017). Here we only briefly survey the instrument design before carefully addressing the installation and use at the synchrotron. All studies were performed at BL 4-3 of the SSRL. This is a wiggler beamline with a double Si(111) monochromator. The incident flux at the S *K*-edge was approximately $1 \times 10^{12}\ \mathrm{s}^{-1}$, as measured by upstream gas ionization chambers. The beam size was approximately 10 mm (horizontal) by 0.5 mm (vertical). A photograph of the installed spectrometer at BL 4-3 is given in Fig. 2(*a*) and shows an interesting constraint: BL 4-3 is a side-station with only ~7 cm clearance between the beam and the hutch wall. The small size of the helium/vacuum chamber of the DRR spectrometer fortuitously accommodates this tight clearance when rotated so that the optic is in the preferred horizontal direction to suppress elastic scattering. The spectrometer was directly attached to the helium-filled beampipe using a flexible bellows without any intervening window. A slow flow of helium was used to continually flush the system.

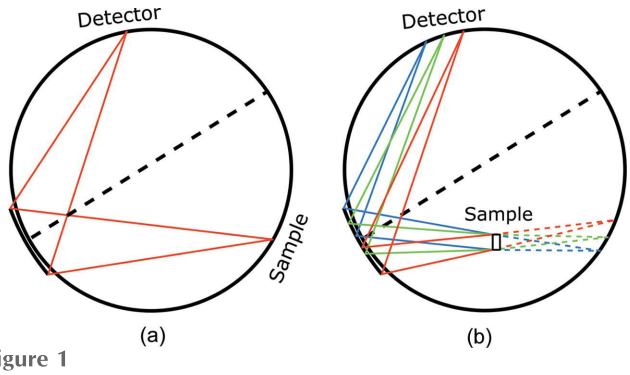

Figure 1
Rowland circle diagram of (*a*) a point-focusing spectrometer design and (*b*) a DRR design. In the point-focusing case, the sample and detector must be scanned across the circle to measure the spectrum, but, in the DRR case, the entire spectrum is collected at once with a position-sensitive detector. Placing the detector tangent to the Rowland circle removes source-size broadening effects.

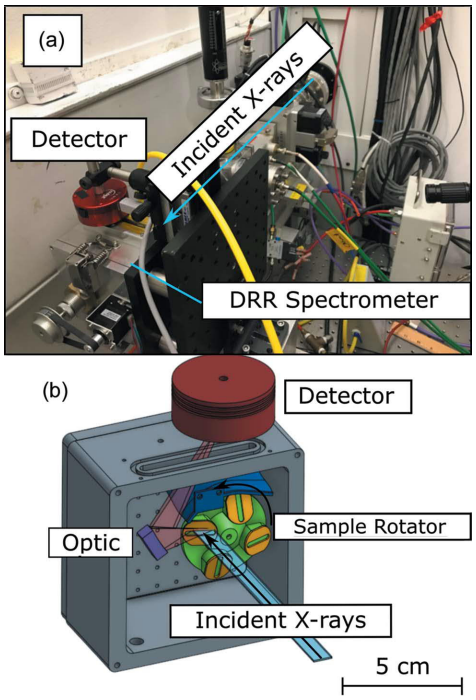

Figure 2
(*a*) Image of the DRR X-ray spectrometer mounted at BL 4-3 of SSRL. (*b*) A computer-aided design (CAD) rendering of the interior of the spectrometer, showing the incident beam (blue), sample holder (yellow), sample rotator (green), focusing optic (purple) and sample emission (red). Note that the orientation changes between the two subfigures.

A rendering of the spectrometer in the as-installed orientation is given in Fig. 2(*b*). As shown, the sample footprint (preparation described below) was designed to match the unfocused beam spot. Fluorescence from the sample illuminates the 10 cm-radius Si (111) cylindrical analyzer crystal (XRSTech) and is detected by a home-made spectroscopic X-ray camera (Holden *et al.*, 2017; Holden, Hoidn *et al.*, 2018) that is positioned on the Rowland circle defined by the analyzer. The spectroscopic nature of the camera allows energy-windowing of each detected event to reject stray scatter backgrounds at energies far from the anticipated fluorescence line. The camera has an energy resolution of 86 eV for P $K\alpha$ emission (2014 eV) which allows for the separation of the emission line of interest from other fluorescence in most cases. However, the camera also limits the upper energy range of the spectrometer, as the quantum efficiency of the detector decreases with increasing energy. The efficiency is approximately 50% near sulfur $K\beta$ (2.5 keV), 35% near uranium $M\beta$ (3.7 keV) and drops to <10% above 6 keV (Holden, Hoidn *et al.*, 2018). The X-ray camera, sample turret motor and camera motors were run using a user laptop. Coordination between the user laptop and the beamline software was straightforward, using a TTL gate signal to trigger the camera software on the laptop, as is typically used for other detectors.

Fine alignment of the spectrometer was performed at the beamline. First, the energy of the incident X-rays is tuned to the maximum of the white line of the absorption spectrum of the sample (*e.g.* incident energy 2472 eV for $Na_2S_2O_3$). The position of the spectrometer perpendicular to the beam was adjusted by motorized stages to achieve maximal count rates. Then the camera position is optimized to focus the emission spectrum in the center of the camera. When complete, this alignment finds a full width at half-maximum of 0.81 eV for the elastic scattering peak at 2472 eV; see Section 3 for further discussion of performance.

2.2. Sample preparation

$(PPh_4)_2WS_4$ was synthesized as previously described and isolated as single crystals (Lang *et al.*, 2002; Olson *et al.*, 2014); meanwhile, $Na_2S_2O_3$ was obtained commercially and used as received. These compounds were then used to prepare samples on the benchtop for analysis by S *K*-edge spectroscopic analyses on BL 4-3 of SSRL. Two sets of samples were prepared, one for X-ray absorption spectroscopy (XAS) and another for RIXS measurements. Care was taken to minimize self-absorption in the XAS samples (samples were mechanically ground and the analyte dispersed as a thin film on low-sulfur tape) so that total fluorescence yield (TFY) obtained by XAS could be used to correct for self-absorption in the RIXS data. The reason two separate samples are needed is that a TFY spectrum free of self-absorption requires a very thin sample, but RIXS requires as many X-ray emission events as possible, and so a thick sample allows for the collection of data in a reasonable time-frame.

The XAS samples were mounted in aluminium sample holders consisting of simple 1 mm-thick aluminium plates with 5 mm × 20 mm slots. Single-sided tape (40 mm), confirmed by X-ray fluorescence spectroscopy to contain low concentrations of sulfur, was fixed to the downstream side of the holder. Analytes were prepared by finely grinding the sample for 2 min in polystyrene canisters with Teflon pestles using an automatic grinder to obtain a homogeneous fine powder. The sample canisters and pestles showed no detectable S by X-ray fluorescence analysis. The finely divided powder was then uniformly dispersed onto the single-sided tape using a Winsor & Newton paintbrush, which did not contain significant amounts of S as determined by independent S *K*-edge XAS analysis. The sample holder was sealed by adhering a 4 mm-thick polypropylene window (SPEX CertiPrep 3525 Ultralene) to the aluminium plate double-sided tape, the latter slotted to match the front side of the sample holder. The X-ray absorption spectra (XAS) samples were inserted into a sample chamber flushed continuously with helium gas.

RIXS samples were prepared by loading the finely ground samples (approximately 60 mg) into RIXS sample holders. These were 1 mm-thick aluminium plates with a 5 mm × 20 mm slots, *i.e.* similar to the XAS holder. They differ in that the downstream side of the plates were sealed with five layers of single-sided low-S content tape. This thick backing prevented transmission to (and subsequent fluorescence of) the sample turret, thus decreasing potential backgrounds. The upstream side of the holder was equipped with a polypropylene window (4 µm) that was secured to the holder with double-sided tape. Sample holders were fixed to the sample rotator with double-sided tape.

The $Cs_2UO_2Cl_4$ compound was prepared as previously described (Watkin *et al.*, 1991) and its structure was confirmed by single-crystal X-ray diffraction. It should be emphasized that uranium is radioactive and represents a hazard to human health. These experiments should only be performed in facilities with the proper controls in place to handle radioactive material. The sample was prepared in an argon-filled glovebox and finely ground for 2 min in polystyrene canisters with Plexiglass pestles using a Wig-L-Bug grinder. A 5 mm × 20 mm × 1 mm aluminium well was filled with sample (approximately 50 mg). The back of the sample holder was sealed with a single layer of 25 µm-thick Kapton tape. The front of the holder was sealed with a piece of polypropylene (4 µm-thick). The entire sample holder was covered with a second layer, which consisted of a single layer of 25 µm-thick Kapton tape on the back and a second layer of polypropylene (4 µm-thick) on the front. This envelope provided a second layer of containment. The sample assembly was then shipped to SSRL.

2.3. Data collection and operating conditions

Sulfur *K*-edge total fluorescence yield X-ray absorption spectra (TFY-XAS) were collected within the LANL Tender X-ray Chamber at BL 4-3 under dedicated operating conditions (3.0 GeV, 500 mA) for normalization of the S RIXS

spectra. The chamber and incident flux (I_0) gas ionization detector were separated from the beam pipe by a beryllium window. Sample fluorescence was monitored using a partially depleted series charged particle detector with a 5000 mm^2 active area (Mirion Technologies, model PD5000-75-500AM). The energy scale was calibrated by setting the energy of the pre-edge maximum of a thin $Na_2S_2O_3$ sample to 2742.02 eV or a thin KCl sample at 3608.4 eV (Solomon *et al.*, 2005). These total fluorescence yield measurements were only used as a point of comparison to carry out the self-absorption correction described in Section 2.4. Beam damage was ruled out by comparing three short scans (1 min each) on each compound (2460–2490 eV for S and 3542–3738 eV for U).

All RIXS measurements were carried out under dedicated operating conditions (3.0 GeV, 500 mA) at BL 4-3 of SSRL. Sulfur X-ray emission measurements used a cylindrically bent Si (111) optic at median Bragg angles of 58.9° ($K\alpha$) and 54.5° ($K\beta$), respectively. Uranium $M\beta$ RIXS measurements used a cylindrically bent Ge (220) optic at a median Bragg angle of 68.0°. Incident energy scales were calibrated to the pre-edge maximum of a thin $Na_2S_2O_3$ sample at 2472.02 eV and a thin KCl sample at 3608.4 eV for sulfur and uranium samples, respectively. Emission energy scales of sulfur were calibrated to the highest energy peak of non-resonant $Na_2S_2O_3$ emission at 2309.12 eV, which corresponds to $K\alpha_1$ of the S^{6+} atom. We expect this to be similar to S^{6+} compounds measured previously, which showed little variation, and matched this peak to the 2309.12 eV S $K\alpha_1$ of Na_2SO_4 (Alonso-Mori *et al.*, 2009). For S $K\beta$ RIXS, we used the elastic scatter peak of $Na_2S_2O_3$ at 2472 eV (with an incident X-ray energy of 2472 eV) for calibration, and for U $M\beta$ we used the non-resonant $UO_2Cl_4^{2-}$ emission at 3339.8 eV (Vitova *et al.*, 2017). For sulfur, measurement times were 5 min in total per incident energy point with a total RIXS plane measurement time of 5 h. For $UO_2Cl_4^{2-}$, measurement times were 80 s per incident energy point with a total RIXS plane measurement time of just under 2 h. We ruled out beam damage as we observed no changes during several scans over the incident energy range. For sulfur measurements, this was a series of eight approximately 40 min-long scans over the incident energy range 2460–2490 eV. For $UO_2Cl_4^{2-}$, this was only two 40 min-long scans over the incident energy range 3700–3800 eV.

2.4. Data processing and self-absorption corrections

Because a thick sample is necessary to collect a RIXS plane in a reasonable amount of time, and we wished to take cuts in the RIXS plane to obtain high-energy resolution fluorescence detection spectra, self-absorption corrections are needed. First, we define an effective absorption coefficient $\mu_{\rm RIXS}(E_{\rm i})$ as the sum over the emitted energy of the measured RIXS intensity, *i.e.* a partial fluorescence yield (PFY) measurement of the X-ray absorption for the particular fluorescence energy range being studied,

$$\mu_{\rm RIXS}(E_{\rm i}) = \sum_{E_{\rm e}} I_{\rm RIXS}(E_{\rm i},\ E_{\rm e}), \qquad (1)$$

where $I_{\rm RIXS}(E_{\rm i},\ E_{\rm e})$ is the intensity of the measured RIXS spectrum at emitted energy $E_{\rm e}$ and incident energy $E_{\rm i}$. Under the assumption that the PFY signal on the thick RIXS sample is roughly proportional to a total fluorescence yield (TFY) signal on the same (thick) sample, we see that the sample self-absorption can be corrected by the ratio of a TFY measurement on a thin sample (*i.e.* not exhibiting self-absorption) and the measured PFY signal integrated from the RIXS,

$$I_{\rm Corrected}(E_{\rm i},\ E_{\rm e}) = I_{\rm RIXS}(E_{\rm i}, E_{\rm e}) \frac{\mu_{\rm TFY}(E_{\rm i})}{\mu_{\rm RIXS}(E_{\rm i})}, \qquad (2)$$

where $I_{\rm Corrected}(E_{\rm i},\ E_{\rm e})$ is the final corrected RIXS spectrum and $\mu_{\rm TFY}(E_{\rm i})$ is the XAS spectrum collected on a thin sample in fluorescence mode. We can see that summing over the emitted energy of the corrected RIXS spectrum yields the TFY absorption spectrum on a thin sample, as desired. This self-absorption correction was applied to all RIXS datasets, and results in corrections of less than 20%. The corrected $[\mu_{\rm RIXS}(E_{\rm i})]$ and uncorrected $[\mu_{\rm TFY}(E_{\rm i})]$ spectra are shown in Fig. S1 of the supporting information. In general, self-absorption on a normalized spectrum has the effect of 'flattening' the spectrum towards a value of 1, which is what we see here. It should also be noted that it is possible that the thin samples prepared are not fully free of self-absorption effects. A total electron yield (TEY) measurement could be a good way to perform this measurement in the future to ensure the comparison spectrum is not self-absorbed.

Other data processing was minimal. Several of the collected spectra had hot pixels which were filtered. Each emission spectrum was normalized to the time-integrated incident X-ray intensity measured at the I_0 ion chamber. XAS data were normalized to an edge-step of unity (excluding the uranium data which were peak-normalized) using the *Athena* and the *Demeter* packages (Ravel & Newville, 2005).

3. Results and discussion

It is useful to briefly describe the underlying physics of the S $K\alpha$ RIXS experiment. A naïve description involves two-steps. There is an excitation to an intermediate excited state followed by characterization of the relaxation process to a final excited state. Using orbital descriptions (Fig. 3), the excitation involves bound-state transitions between S 1*s* orbitals and virtual (unoccupied) orbitals that contain, for example, some degree of S 3*p* character for excitations near the S *K*-edge. The emission involves electronic relaxation from the S 2*p* orbitals to the S 1*s* orbitals. Hence, for a free S^{6+} ion (no ligand field), the experiment involves electronic excitation of the $1s^2\ 2s^2\ 2p^6\ 3p^0$ ground state to the intermediate $1s^1\ 2s^2\ 2p^6\ 3p^1$ excited electronic state followed by relaxation to the $1s^2\ 2s^2\ 2p^5\ 3p^1$ final excited state.

Fig. 4 shows experimental S $K\alpha$ RIXS data from two compounds, $(PPh_4)_2WS_4$ and $Na_2S_2O_3$, with the intensity plotted as a function of incident energy and energy transfer (incident energy minus emitted energy, Fig. 3). Plotting incident energy versus energy transfer makes it clear that the broadening of the final and intermediate states are indepen-

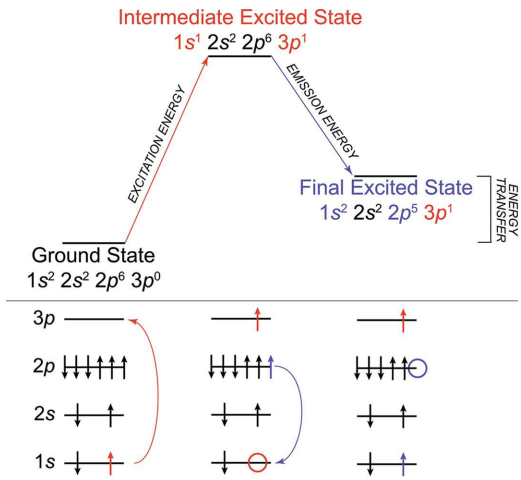

Figure 3
A general description for electron transfer processes for a free S^{6+} ion during the S $K\alpha$ RIXS spectroscopy experiment.

dent, and that a diagonal cut across the RIXS plane at constant emission energy can yield an XAS-like spectrum where the core-hole lifetime broadening is suppressed (Glatzel & Bergmann, 2005; De Groot *et al.*, 2002; Hämäläinen *et al.*, 1991); this is the basis for high-energy resolution fluorescence detection (HERFD), originally known as partial fluorescence yield X-ray absorption near-edge spectroscopy.

WS_4^{2-} is a well studied standard for benchmarking this DDR spectrometer because its S *K*-edge XAS spectrum is well characterized (Olson *et al.*, 2014; Müller *et al.*, 1994; Wittneben *et al.*, 1989; Frank *et al.*, 1987). The spectrum contains a pair of pre-edge features that result from excitation of S 1*s* electrons to unoccupied molecular orbitals of *e* and t_2 symmetry (Olson *et al.*, 2014). In contrast, the RIXS spectrum from WS_4^{2-} has not been reported previously. It contains a quartet of low-energy peaks whose final excited states (energy transfer) are approximately 163 eV above the ground state incident energies near 2473 eV. The four features are best described as a set of pairs, one with incident energies near 2470 eV and a second set with excitation energies near 2472 eV. Within each pair, a 1 eV difference in energy transfer distinguishes the two peaks and is the expected $K\alpha_{1,2}$ spin orbit splitting.

Moving to $Na_2S_2O_3$, thiosulfate has two distinct sulfur sites, one sulfate-like S^{6+} and one sulfide-like S^{2-}. These different oxidation states have XAS spectra with edge steps at 2482 eV and 2470–2473 eV, respectively, and XES spectra with $K\alpha_1$ peak locations at 2309.1 eV and 2307.8 eV, respectively (Alonso-Mori *et al.*, 2009). We see one pair of low-energy features, identified at an incident energy of 2472 eV and an energy transfer of ~164 eV corresponding to the $K\alpha_{1,2}$ peaks of the sulfide-like site. At higher energy (2482 eV incident and 170 eV energy transfer), the sulfate-like site can also be excited and two additional pairs of peaks were observed. The emission energy of these peaks is higher, and so these peaks fall below the dotted line corresponding to a constant S^{2+} $K\alpha_1$ emission energy of 2307.8 eV. Although RIXS of these compounds has not previously been reported, the signal quality above the background of our results compares favorably with prior work on other sulfur compounds (Kavčič *et al.*, 2012, 2016; Robba *et al.*, 2017; Marchenko *et al.*, 2015).

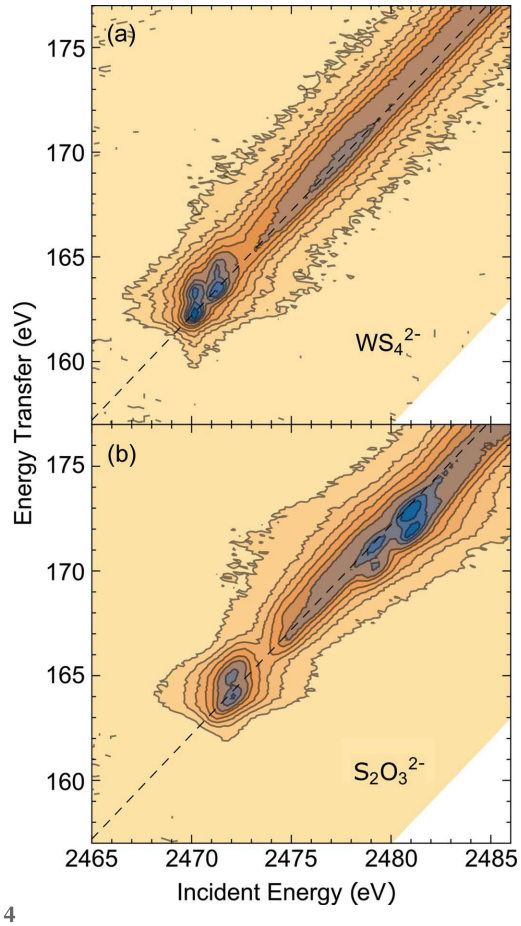

Figure 4
Contour plots showing the RIXS measurements from (*a*) $(PPh_4)_2WS_4$ and (*b*) $Na_2S_2O_3$. Each plot shows energy transfer (S *K*-edge X-ray absorption energies minus the $K\alpha_1$, $K\alpha_2$ X-ray emission energies) versus the S *K*-edge X-ray absorption energy. Dashed lines indicate the diagonal cuts used for HERFD spectra. These lines are set at the maximum of the pre-edge feature.

In Fig. 5, we present $K\alpha$ HERFD cuts (emission energy 2307.8 eV) through the RIXS plane for both compounds and compare those spectra with the TFY results collected for normalization. The dashed line in Fig. 4 shows the constant emission energy (2307.8 eV) cuts taken to obtain the HERFD spectra. This emission energy was chosen to be the maximum of the resonant emission at the pre-edge so that the pre-edge features line up at the same positions as in the XANES spectrum. The HERFD spectra were produced by integrating over 0.1 eV emission energy. In both cases, there is a modest improvement in energy resolution over the XAS data, similar to previous results (Kavčič *et al.*, 2016) on SO_3^{2-}. The magnitude of the energy-resolution improvement can be estimated as shown by De Groot *et al.* (2002), yielding a HERFD energy resolution of 0.43 eV, only slightly smaller than the S 1*s* lifetime broadening of 0.53 eV. The limited improvement is because the experimental resolution is larger than the 1*s* lifetime broadening. A detector with a low-energy resolution would be equivalent to a total fluorescence yield measurement (0.53 eV broadening in this case), and, as the

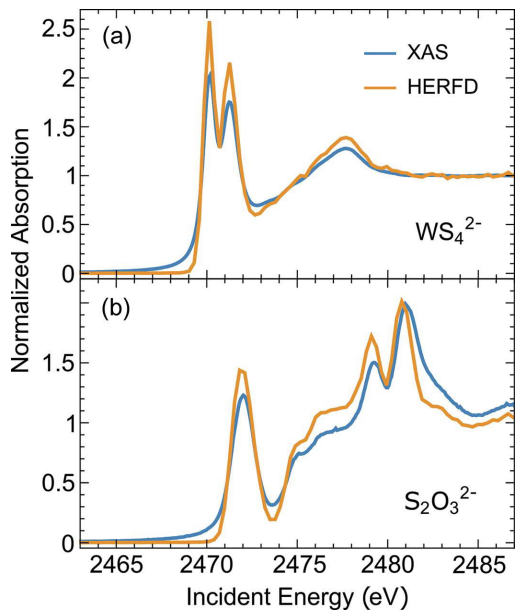

Figure 5
HERFD (orange) and TFY-XAS (blue) spectra for both (*a*) $(PPh_4)_2WS4$ and (*b*) $Na_2S_2O_3$. TFY-XAS spectra are collected in fluorescence mode on a thin sample and HERFD spectra are a diagonal cut of the RIXS plane. In both cases, the HERFD spectrum shows modest improvement in the energy resolution with respect to the TFY-XAS spectrum.

energy resolution of the detector improves, the broadening of the HERFD spectrum decreases.

As a more stringent test of the sensitivity of the spectrometer at BL 4-3, we also measured S $K\beta$ RIXS of NaS_2O_3, shown in Fig. 6. The S $K\beta$ RIXS experiment is similar to the S $K\alpha$ RIXS process described above (Fig. 3) in that it also involves an initial electronic excitation from the 1*s* orbital to an intermediate excited state that involves the S 3*p* valence orbitals (see Fig. 7). It differs in that progression to the final excited state involves a higher energy $3p \rightarrow 1s$ transition, rather than the $2p \rightarrow 1s$ process in S $K\alpha$ RIXS. As a result, the

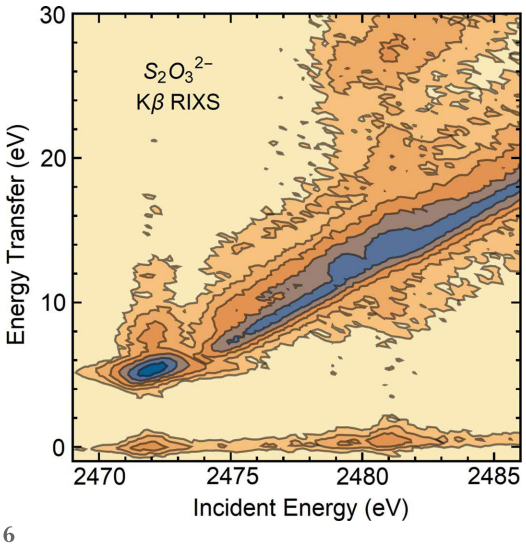

Figure 6
Contour plot of S $K\beta$ RIXS collected on $Na_2S_2O_3$. As in Fig. 4, X-ray intensity is plotted against the incident energy and energy transfer (incident emitted energy).

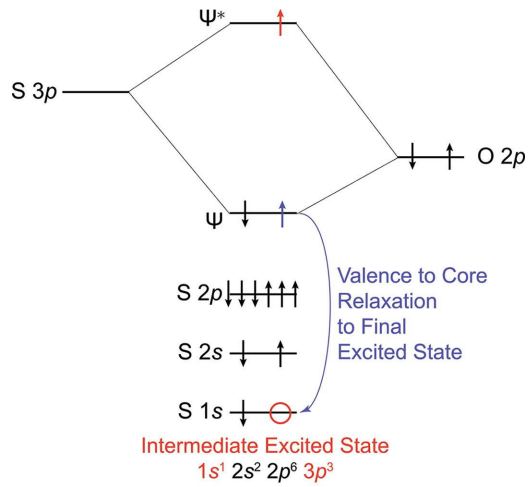

Figure 7
A general description for the valence-to-core relaxation process that occurs during the S $K\beta$ RIXS spectroscopy experiment.

S $K\beta$ RIXS technique directly probes the occupied valence orbitals and the S $K\beta$ RIXS spectra is more heavily influenced by the sulfur chemical environment than the $K\alpha$ RIXS spectra. Another difference is associated with emission intensity. For each 1*s* core hole created, S $K\beta$ X-ray emission is more than ten times less likely than $K\alpha$ emission (Ertuğral *et al.*, 2007; Salem *et al.*, 1974), so count rates are low (approximately total 50 total counts s^{-1}). Fortunately, the detected background is also correspondingly low.

The $S_2O_3^{2-}$ S $K\beta$ RIXS spectrum is shown in Fig. 6 and RXES spectra are shown in Fig. 8. The RIXS spectrum contains a strong feature with an incident energy of 2472 eV and 6 eV in energy transfer, the latter of which tails to approximately 12 eV. At higher incident energy, there are a series of peaks that also tail in energy transfer by about 6 eV. The RXES cuts shown are split into two groups: ones with an excitation energy below the sulfate-like edge of 2482 eV (A, B) and those with an excitation energy above that edge (C, D). The main difference is that spectra A and B show no $K\beta'$ peak, but spectra C and D do at approximately 2453 eV emission energy. This peak has been attributed to transitions involving a molecular orbital of primarily oxygen character (Alonso-Mori *et al.*, 2010), and so when the incident X-ray energy is insufficient to excite the S^{6+} 1*s* electron we would expect to only see emission from the S^{2-} site, and so there is no $K\beta'$ at the lower energies (as this sulfur site is not bonded to oxygen). The elastic scattering present in the $K\beta$ RIXS measurement [highest energy peak of Fig. 8(*b*) in each case] provides an opportunity to measure the energy resolution of the spectrometer, as this peak should only be broadened by the energy resolution of the beamline monochromator. With an incident energy of 2472 eV, the elastic scattering peak in the S $K\beta$ RIXS study showed a full width at half-maximum of 0.81 eV. Allowing for the ~0.3 eV energy resolution of the monochromator, we infer a spectrometer energy resolution of ~0.75 eV. While slightly inferior to that of other spectrometers in this energy range (Kavčič *et al.*, 2012), the results

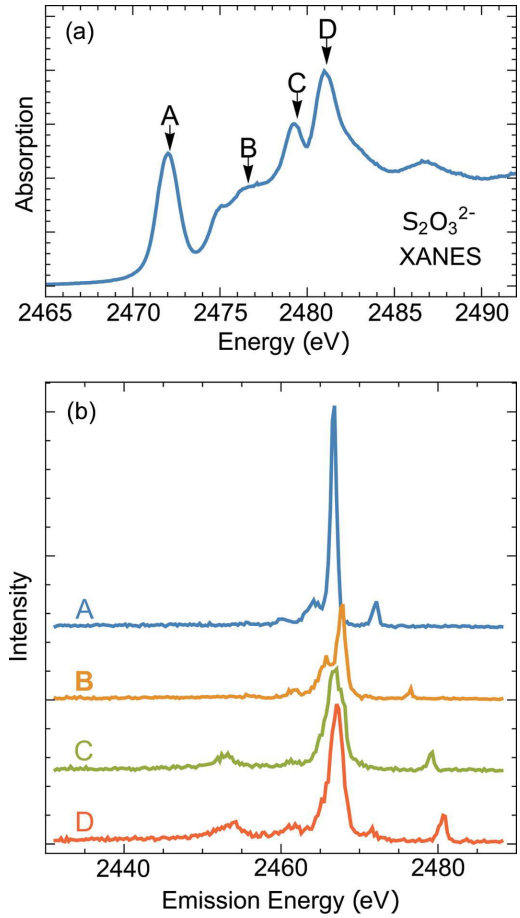

Figure 8
Resonant XES (constant incident energy) cuts of the $Na_2S_2O_3$ $K\beta$ RIXS plane. Spectra in (*b*) correspond to the incident energies selected in (*a*). The highest energy emission peak is elastic scatter where the emission energy equals the incident energy.

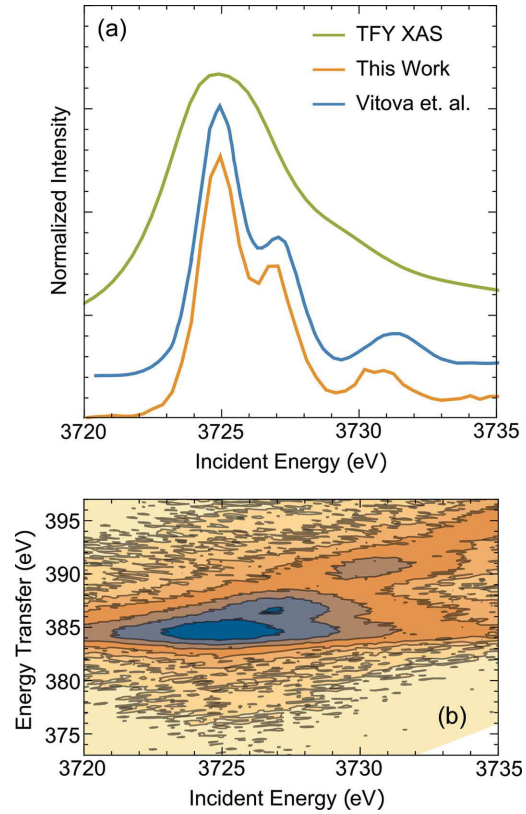

Figure 9
(*a*) U M_4-edge HERFD cut of $UO_2Cl_4^{2-}$ collected using both the DRR spectrometer (orange) and the measurements by Vitova *et al.* (2017) (blue) at ANKA-INE, and a TFY XAS measurement on a thin sample (green). Spectra are offset for clarity. (*b*) U $M\beta$ RIXS plane collected using the DRR spectrometer. Spectra are offset for clarity and normalized to peak intensity for better comparison.

below indicate that this resolution suffices for a broad range of future applications.

This energy resolution, however, is extremely effective for the slightly higher energy study of the U $M\beta$ emission from $Cs_2UO_2Cl_4$ (see Fig. 9). The study of actinide *M*-edge XAS has been stymied by the large (3.5 eV) core-hole broadening of the 3*d* electrons which limits the ability of X-ray absorption to distinguish features. Therefore, RIXS of actinide materials has great promise as it resolves features at energy scales less than the core-hole lifetime broadening. This was done to great effect in UO_2^{2+} (Kvashnina *et al.*, 2014; Vitova *et al.*, 2013, 2015, 2017), which revealed several previously unresolved $3d \rightarrow 5f$ transitions.

Of particular significance – especially for the experiments reported herein – is the study by Vitova *et al.* (2017) using U $M\beta$ RIXS to investigate the uranium electronic structure. The experiment involves core-to-core electron transitions involving a U $3d \rightarrow$ U $5f$ excitation followed by relaxation of a core U 4*f*-electron (Fig. 10). Using our spectrometer, we were able to obtain a spectrum in 2 h on 60 mg of $Cs_2UO_2Cl_4$ sample using the unfocused BL at SSRL (4-3) which reproduces Vitova's spectrum collected with a scanning, point-focusing Rowland spectrometer at the INE actinide beamline of Angströmquelle Karlsruhe (ANKA) (Kleymenov *et al.*, 2011; Zimina *et al.*, 2017). A HERFD spectrum was obtained by averaging a 0.1 eV-wide slice of the RIXS plane at an emission energy of 3340.3 eV, the maximum of the resonant emission. The spectrum contains three primary peaks with incident energies of approximately 3723 eV, 3728 eV and 3730 eV separated by about 2 eV in energy transfer energy, corresponding to the splitting of the unoccupied 5*f* states into δ/φ non-bonding and π- and σ-antibonding orbitals. The data of Fig. 9 have been shifted by 1.8 eV to align the two spectra at the energy of the first peak. We attribute the difference in

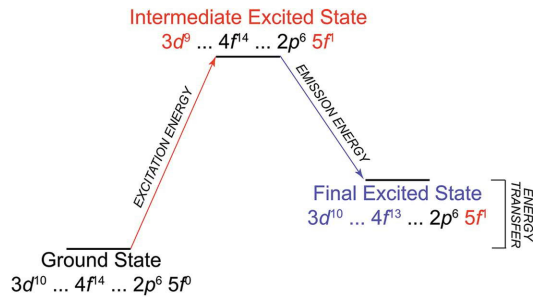

Figure 10
A general description for the core-to-core processes occurring during the U $M\beta$ RIXS spectroscopy experiment.

energy scales to the difference in calibration methods between the two experiments. To better align with other previous *M*-edge studies (Kraft *et al.*, 2011), our $UO_2Cl_4^{2-}$ spectra were calibrated to the pre-edge maximum of a KCl XAS spectrum at 3608.4 eV and Vitova *et al.* (2017) calibrated to the white line of a UO_2 spectrum at 3725.2 eV. Aside from the energy scale mismatch, the results collected here agree well with those presented by Vitova *et al.* (2017). The uranyl of Vitova *et al.* (2017) shown in Fig. 9 is UO_2^{2+} in solution, which is a different uranyl coordination environment than the solid $CsUO_2Cl_4$ measured here. The difference in σ-antibonding peak position could be attributed to differences in the axial U—O bond distance, as laid out by Vitova *et al.* (2018) and Podkovyrina *et al.* (2016). In those works, it was shown that a longer U—O axial bond corresponds to a lower energy σ-antibonding peak. There is a longer axial U—O bond distance in $Cs_2UO_2Cl_4$ than in aqueous UO_2^{2+} (Allen *et al.*, 1997), so this shift is at least in qualitative agreement with previous results. In comparing the two experiments, one major difference is that to collect a HERFD spectrum the focusing Rowland spectrometer only collects at the peak emission energy of the U $M\beta$, and so the HERFD spectrum was collected in 1 s per point. In contrast, the experiment described here required 80 s per point collection time, but the whole RIXS plane was collected.

Looking to the future, there are several directions for improved performance or broader range of application. First, finer energy resolution or improved solid angle of collection can be achieved with a Johansson (bent and ground) optic; this crystal motif eliminates the Johann error resulting from the edges of the optic not sitting on the Rowland circle (Bergmann & Cramer, 1998), especially when working at Bragg angles farther from backscatter. Second, as pointed out previously, the compact design of the spectrometer suggests its installation in a glovebox at an end-station (Holden *et al.*, 2017). In this way, RIXS measurements could be performed on air-sensitive samples without the samples ever leaving a controlled atmosphere. This also has particular relevance for actinide chemistry, where the glovebox could act as a layer of containment, allowing for more complex experiments and easier facilitation of on-site chemistry. Finally, the DRR design could be modified to use larger radii optics. Although this would increase the footprint of the instrument, it could allow for doubly focusing optics which would improve efficiency and count rates.

4. Conclusions

We have demonstrated that the miniature dispersive Rowland refocusing spectrometer offers an opportunity to perform advanced photon-in/photon-out X-ray spectroscopies (XES, RIXS, HERFD) using a portable instrument which is suitable for use with unfocused beamlines and large beam spots. The compatibility of this spectrometer with large beam spots permits intentionally increasing spot size to reduce radiation dose and subsequent damage to sensitive samples. Collection times are manageable (several hours for a RIXS plane) and low background allows for the measurement of low-intensity X-ray emission lines. Results compared favorably with previous sulfur RIXS measurements made with a dispersive spectrometer design and also reproduced prior measurements on $UO_2Cl_4^{2-}$ made with a focusing spectrometer. As such, we anticipate that this spectrometer design will expand the availability of these advanced spectroscopies, especially in this energy range, which is, at present, only possible at a small number of beamlines.

Funding information

This work was supported by the US Department of Energy (DOE), Office of Science, Office of Basic Energy Sciences, Heavy Element Chemistry program. LANL, an affirmative action/equal opportunity employer, is managed by Triad National Security, LLC, for the NNSA of the US Department of Energy (contract No. 89233218CNA000001). We also acknowledge the named fellowship program Hoffman Distinguished Postdoctoral Fellowship (SKC). Partial support also came from the Joint Plasma Physics Program of the National Science Foundation and the DOE (grant No. DE-SC0016251 awarded to WHM, ORH and GTS). Use of the Stanford Synchrotron Radiation Lightsource, SLAC National Accelerator Laboratory, was supported by the US Department of Energy, Office of Science, Office of Basic Energy Sciences (contract No. DE-AC02-76SF00515). The SSRL Structural Molecular Biology Program is supported by the DOE Office of Biological and Environmental Research, and by the National Institute of Health, National Institute of General Medical Sciences (including P41GM103393).

References

Allen, P. G., Bucher, J. J., Shuh, D. K., Edelstein, N. M. & Reich, T. (1997). *Inorg. Chem.* **36**, 4676–4683.

Alonso-Mori, R., Paris, E., Giuli, G., Eeckhout, S. G., Kavčič, M., Žitnik, M., Bučar, K., Pettersson, L. G. M. & Glatzel, P. (2009). *Anal. Chem.* **81**, 6516–6525.

Alonso-Mori, R., Paris, E., Giuli, G., Eeckhout, S. G., Kavčič, M., Žitnik, M. Bučar, K., Pettersson, L. G. M. & Glatzel, P. (2010). *Inorg. Chem.* **49**, 6468–6473.

Bergmann, U. & Cramer, S. P. (1998). *Proc. SPIE*, **3448**, 198.

Butorin, S. M. (2000). *J. Electron Spectrosc. Relat. Phenom.* **110–111**, 213–233.

Cossairt, B. M., Stein, J. L., Holden, W. M. & Seidler, G. T. (2018). *SID Symp. Dig. Tech. Pap.* **49**, 21–24.

Dolgih, V. E., Cherkashenko, V. M., Kurmaev, E. Z., Goganov, D. A., Ovchinnikov, E. K. & Yarmoshienko, Y. M. (1984). *Nucl. Instrum. Methods Phys. Res.* **224**, 117–119.

Ertuğral, B., Apaydın, G., Çevik, U., Ertuğrul, M. & Kobya, A. İ. (2007). *Radiat. Phys. Chem.* **76**, 15–22.

Frank, P., Hedman, B., Carlson, R. M. K., Tyson, T. A., Roe, A. L. & Hodgson, K. O. (1987). *Biochemistry*, **26**, 4975–4979.

Gamboa, E. J., Huntington, C. M., Trantham, M. R., Keiter, P. A., Drake, R. P., Montgomery, D. S., Benage, J. F. & Letzring, S. A. (2012). *Rev. Sci. Instrum.* **83**, 10E108.

Glatzel, P. & Bergmann, U. (2005). *Coord. Chem. Rev.* **249**, 65–95.

Glenzer, S. H., Gregori, G., Lee, R. W., Rogers, F. J., Pollaine, S. W. & Landen, O. L. (2003). *Phys. Rev. Lett.* **90**, 175002.

Glenzer, S. H. & Redmer, R. (2009). *Rev. Mod. Phys.* **81**, 1625–1663.

Groot, F. de & Kotani, A. (2008). *Core Level Spectroscopy of Solids*, in *Advances in Condensed Matter Science*. Boca Raton: CRC Press.

Groot, F. M. F. de, Krisch, M. H. & Vogel, J. (2002). *Phys. Rev. B*, **66**, 195112.

Hämäläinen, K., Siddons, D. P., Hastings, J. B. & Berman, L. E. (1991). *Phys. Rev. Lett.* **67**, 2850–2853.

Hoidn, O. R. & Seidler, G. T. (2014). *Phys. Plasmas*, **21**, 012707.

Holden, W. M., Hoidn, O. R., Ditter, A. S., Seidler, G. T., Kas, J., Stein, J. L., Cossairt, B. M., Kozimor, S. A., Guo, J., Ye, Y., Marcus, M. A. & Fakra, S. (2017). *Rev. Sci. Instrum.* **88**, 073904.

Holden, W. M., Hoidn, O. R., Seidler, G. T. & DiChiara, A. D. (2018). *Rev. Sci. Instrum.* **89**, 093111.

Holden, W. M., Seidler, G. T. & Cheah, S. (2018). *J. Phys. Chem. A*, **122**, 5153–5161.

Hudson, A. C., Stolte, W. C., Lindle, D. W. & Guillemin, R. (2007). *Rev. Sci. Instrum.* **78**, 053101.

Hudson, L. T., Henins, A., Deslattes, R. D., Seely, J. F., Holland, G. E., Atkin, R., Marlin, L., Meyerhofer, D. D. & Stoeckl, C. (2002). *Rev. Sci. Instrum.* **73**, 2270–2275.

Huotari, S., Pylkkänen, T., Verbeni, R., Monaco, G. & Hämäläinen, K. (2011). *Nat. Mater.* **10**, 489–493.

Kavčič, M., Bučar, K., Petric, M., Žitnik, M., Arčon, I., Dominko, R. & Vizintin, A. (2016). *J. Phys. Chem. C*, **120**, 24568–24576.

Kavčič, M., Budnar, M., Mühleisen, A., Gasser, F., Žitnik, M., Bučar, K. & Bohinc, R. (2012). *Rev. Sci. Instrum.* **83**, 033113.

Kleymenov, E., van Bokhoven, J. A., David, C., Glatzel, P., Janousch, M., Alonso-Mori, R., Studer, M., Willimann, M., Bergamaschi, A., Henrich, B. & Nachtegaal, M. (2011). *Rev. Sci. Instrum.* **82**, 065107.

Kraft, S. J., Williams, U. J., Daly, S. R. J., Schelter, E., Kozimor, S. A., Boland, K. S., Kikkawa, J. M., Forrest, W. P., Christensen, C. N., Schwarz, D. E., Fanwick, P. E., Clark, D. L., Conradson, S. D. & Bart, S. C. (2011). *Inorg. Chem.* **50**, 9838–9848.

Kritcher, A. L., Döppner, T., Fortmann, C., Landen, O. L., Wallace, R. & Glenzer, S. H. (2011). *High. Energ. Density Phys.* **7**, 271–276.

Kvashnina, K. O., Kvashnin, Y. O. & Butorin, S. M. (2014). *J. Electron Spectrosc. Relat. Phenom.* **194**, 27–36.

Labate, L., Köster, P., Levato, T. & Gizzi, L. A. (2012). *Rev. Sci. Instrum.* **83**, 103504.

Lang, J.-P., Kawaguchi, H. & Tatsumi, K. (2002). *J. Chem. Soc. Dalton Trans.* pp. 2573–2580.

Mao, J. Y., Chen, L. M., Hudson, L. T., Seely, J. F., Zhang, L., Sun, Y. Q., Lin, X. X. & Zhang, J. (2012). *Rev. Sci. Instrum.* **83**, 043104.

Marchenko, T., Carniato, S., Journel, L., Guillemin, R., Kawerk, E., Žitnik, M., Kavčič, M., Bučar, K., Bohinc, R., Petric, M., Vaz da Cruz, V., Gel'mukhanov, F. & Simon, M. (2015). *Phys. Rev. X*, **5**, 031021.

Matlis, N. H., Reed, S., Bulanov, S. S., Chvykov, V., Kalintchenko, G., Matsuoka, T., Rousseau, P., Yanovsky, V., Maksimchuk, A., Kalmykov, S., Shvets, G. & Downer, M. C. (2006). *Nat. Phys.* **2**, 749–753.

Müller, A., Wittneben, V., Diemann, E., Hormes, J. & Kuetgens, U. (1994). *Chem. Phys. Lett.* **225**, 359–363.

Olson, A. C., Keith, J. M., Batista, E. R., Boland, K. S., Daly, S. R., Kozimor, S. A., MacInnes, M. M., Martin, R. L. & Scott, B. L. (2014). *Dalton Trans.* **43**, 17283–17295.

Plateau, G. R., Geddes, C. G. R., Thorn, D. B., Chen, M., Benedetti, C., Esarey, E., Gonsalves, A. J., Matlis, N. H., Nakamura, K., Schroeder, C. B., Shiraishi, S., Sokollik, T., van Tilborg, J., Toth, C., Trotsenko, S., Kim, T. S., Battaglia, M., Stöhlker, T. & Leemans, W. P. (2012). *Phys. Rev. Lett.* **109**, 064802.

Podkovyrina, Y., Pidchenko, I., Prüßmann, T., Bahl, S., Göttlicher, J., Soldatov, A. & Vitova, T. (2016). *J. Phys. Conf. Ser.* **712**, 012092.

Ravel, B. & Newville, M. (2005). *J. Synchrotron Rad.* **12**, 537–541.

Robba, A., Vizintin, A., Bitenc, J., Mali, G., Arčon, I., Kavčič, M., Žitnik, M., Bučar, K., Aquilanti, G., Martineau-Corcos, C., Randon-Vitanova, A. & Dominko, R. (2017). *Chem. Mater.* **29**, 9555–9564.

Salem, S. I., Panossian, S. L. & Krause, R. A. (1974). *At. Data Nucl. Data Tables*, **14**, 91–109.

Schülke, W. (2007). *Electron Dynamics by Inelastic X-ray Scattering*. Oxford University Press.

Solomon, E. I., Hedman, B., Hodgson, K. O., Dey, A. & Szilagyi, R. K. (2005). *Coord. Chem. Rev.* **249**, 97–129.

Stein, J. L., Holden, W. M., Venkatesh, A., Mundy, M. E., Rossini, A. J., Seidler, G. T. & Cossairt, B. M. (2018). *Chem. Mater.* **30**, 6377–6388.

Suggit, M., Kimminau, G., Hawreliak, J., Remington, B., Park, N. & Wark, J. (2010). *Rev. Sci. Instrum.* **81**, 083902.

Valdivia, M. P., Stutman, D. & Finkenthal, M. (2015). *Appl. Opt.* **54**, 2577–2583.

Valdivia, M. P., Stutman, D., Stoeckl, C., Mileham, C., Begishev, I. A., Bromage, J. & Regan, S. P. (2018). *Appl. Opt.* **57**, 138–145.

Vitova, T., Denecke, M. A., Göttlicher, J., Jorissen, K., Kas, J. J., Kvashnina, K., Prüßmann, T., Rehr, J. J. & Rothe, J. (2013). *J. Phys. Conf. Ser.* **430**, 012117.

Vitova, T., Green, J. C., Denning, R. G., Löble, M., Kvashnina, K., Kas, J. J., Jorissen, K., Rehr, J. J., Malcherek, T. & Denecke, M. A. (2015). *Inorg. Chem.* **54**, 174–182.

Vitova, T., Pidchenko, I., Biswas, S., Beridze, G., Dunne, P. W., Schild, D., Wang, Z., Kowalski, P. M. & Baker, R. J. (2018). *Inorg. Chem.* **57**, 1735–1743.

Vitova, T., Pidchenko, I., Fellhauer, D., Bagus, P. S., Joly, Y., Pruessmann, T., Bahl, S., Gonzalez-Robles, E., Rothe, J., Altmaier, M., Denecke, M. A. & Geckeis, H. (2017). *Nat. Commun.* **8**, 1–9.

Watkin, D. J., Denning, R. G. & Prout, K. (1991). *Acta Cryst.* C**47**, 2517–2519.

Welter, E., Machek, P., Dräger, G., Brüggmann, U. & Fröba, M. (2005). *J. Synchrotron Rad.* **12**, 448–454.

Wittneben, V., Sprafke, A., Diemann, E., Müller, A., Kuetgens, M., Chauvistré, R. & Hormes, J. (1989). *J. Mol. Struct.* **198**, 525–529.

Woolsey, N. C., Clarke, R. J., Doria, D., Gizzi, L. A., Gregori, G., Hakel, P., Hansen, S. B., Koester, P., Labate, L., Levato, T., Li, B., Makita, M., Mancini, R. C., Pasley, J., Rajeev, P. P., Robinson, A. P. L., Wagenaars, E., Waugh, J. N. & Booth, N. (2011). *High. Energ. Density Phys.* **7**, 105–109.

Zimina, A., Dardenne, K., Denecke, M. A., Doronkin, D. E., Huttel, E., Lichtenberg, H., Mangold, S., Pruessmann, T., Rothe, J., Spangenberg, T., Steininger, R., Vitova, T., Geckeis, H. & Grunwaldt, J. D. (2017). *Rev. Sci. Instrum.* **88**, 113113.